

ARTICLE

<https://doi.org/10.1038/s41467-018-08055-3>

OPEN

Bifurcation-based embodied logic and autonomous actuation

Yijie Jiang¹, Lucia M. Korpas¹ & Jordan R. Raney¹

Many plants autonomously change morphology and function in response to environmental stimuli or sequences of stimuli. In contrast with the electronically-integrated sensors, actuators, and microprocessors in traditional mechatronic systems, natural systems embody these sensing, actuation, and control functions within their compositional and structural features. Inspired by nature, we embody logic in autonomous systems to enable them to respond to multiple stimuli. Using 3D printable fibrous composites, we fabricate structures with geometries near bifurcation points associated with a transition between bistability and monostability. When suitable stimuli are present, the materials swell anisotropically. This forces a key geometric parameter to pass through a bifurcation, triggering rapid and large-amplitude self-actuation. The actuation time can be programmed by varying structural parameters (from 0.6 to 108 s for millimeter-scale structures). We demonstrate this bioinspired control strategy with examples that respond to their environment according to their embodied logic, without electronics, external control, or tethering.

¹Department of Mechanical Engineering and Applied Mechanics, 220 S 33rd St., University of Pennsylvania, Philadelphia, PA 19104, USA. Correspondence and requests for materials should be addressed to J.R.R. (email: raney@seas.upenn.edu)

Responsiveness to environmental stimuli is vital to the function and growth of plant life^{1–6}. Natural morphological changes can take hours (e.g., for dispersal of seeds or environmental adaptation^{3–5}) or less than a second (e.g., the closing of the Venus flytrap, *Dionaea muscipula*, to capture prey^{6,7}). These can also require multiple stimuli or a specific sequence of stimuli. For example, underlying the motion of the Venus flytrap is a complex sequence of sensing and actuation events. Hairs on the leaf lobes must be mechanically stimulated multiple times within 20–30 s for the lobes to close. After partially closing, the plant reassesses the size of any enclosed object and awaits continued stimulation to determine whether to open (to release the object) or to close the rest of the way (to begin digestion)^{7,8}. In traditional mechatronic systems, sensing, actuation, and control are performed electronically. Complex natural logic, however, is embodied in plants more directly through the tools nature has at its disposal: stimuli-induced morphological changes via material composition and the structural (geometric) organization. Recent work in soft robotics has shown the feasibility of embedding control logic in the structure of the robot itself (i.e., microfluidic logic)⁹, opening the door for further nature-inspired control systems, as we explore here.

The ability of a material to adapt to its environment via response to specific stimuli is of interest for numerous applications, from robotics^{10–12} to medicine (e.g., drug delivery^{13,14}). Synthetic active materials have been developed that actuate in response to a variety of stimuli^{15–23}, including chemical cues²⁴, temperature^{10,11,25–31}, light^{12,32–36}, voltage^{37–39}, and water^{40–42}. Each of these stimuli-responsive materials has its own set of strengths as well as practical challenges that need to be addressed for its use in autonomous applications. For example, thermally-activated shape changes, such as those associated with shape-memory polymers^{11,25,27,43,44}, often require mechanical programming and/or large thermal energy transfer to/from the environment. Light- or voltage-responsive materials often require a stimulus of significantly larger magnitude than may be encountered in the ambient environment (e.g., high illumination intensity^{33,45} or high voltage^{37,38}). Actuation via differential swelling (e.g., using bilayers^{42,46,47} or anisotropic composite materials⁴⁰) requires diffusion of stimuli (e.g., solvents), which, depending on sample volume and geometry, can take many minutes due to the intrinsic limits of the speed of diffusion^{40,41}. Moreover, in these examples, the material strain that is induced is a monotonic function of the amount of stimulus that is present, rather than a discrete, sudden morphological change.

The active materials above achieve their responsiveness via composition and microstructure, i.e., via the functionality intrinsic to the specific polymer matrix or (if a composite) to microstructural features, such as fiber alignment. However, the geometric arrangement of the material is also vital to the overall actuation response. Natural systems like plants possess the same speed limits associated with diffusion that synthetic materials do¹. When faster responses are required, however, plants increase the rate of actuation using geometrically defined instabilities⁶, a nonlinear mechanical phenomenon studied extensively^{48–50} in structures, such as beams^{51–57} and shells^{29,46,58}. Snap-through instabilities are associated with rapid morphological changes. These have been used in previous work to enhance the speed of actuation in soft materials, including in response to diffusion. Examples include diffusion-induced actuation via doubly curved beams and multilayer shells with stiffness gradients^{46,57,58}, and structures composed of layers with orthogonal microstructure²⁹.

In this work, we combine anisotropic materials with bistable structures to embody logic (AND, OR, and NAND) in 3D printable composite structures. These structures can be programmed to respond to multiple stimuli and to actuate at specific

times (and in sequences of defined actuation events). We accomplish this by 3D printing self-actuating units consisting of laterally-constrained fibrous composite beams. We design the beams to possess geometries near bifurcation points that govern their stability behavior. The beams swell anisotropically in the presence of suitable stimuli, causing a key geometric parameter to move through a bifurcation point. This triggers rapid and large-amplitude actuation at pre-defined times and in response to multiple stimuli. Specifically, we use *polydimethylsiloxane* (PDMS)-based and *hydrogel*-based materials to respond to non-polar solvents and water, respectively.

Results

General concept. Laterally-constrained beams, depending on their geometric parameters and boundary conditions, can exhibit very different mechanical responses, including cantilever-like bending, snap-through instabilities⁵³, and bistability^{51,52,59}. Each of these behaviors correspond to specific domains in a parameter space defined by beam geometry. For laterally-confined, tilted beams, these key geometric parameters are the inclination angle of the beam (θ) and its slenderness ratio (w/L , where w denotes the beam width and L denotes the beam length) (Fig. 1a). We used finite element simulations (discussed in detail later) to obtain the bistable and monostable energy curves in Fig. 1b (curves I and III, respectively), both with $\theta = 45^\circ$ but with different w/L ratios (corresponding to points I and III in Fig. 1c). A bistable mechanical response is defined by a dual-well potential (Fig. 1b), with each well representing a stable morphology that can be maintained without any applied force or continued input of energy^{51,52}. The two stable configurations are separated by an energy barrier that, if traversed, produces an instability and a rapid snap-through from one stable configuration to the other. The two stable wells are not at the same energy level because in one configuration the beam is unstrained, and in the other it is buckled (associated with strain energy). The size of the energy barrier, i.e., the depth of the second well (E_{out} in Fig. 1b), can be controlled by the geometry of the beams^{51,56,59}. For a fixed θ , as w/L increases (i.e., as the beam becomes wider relative to its length) the energy barrier decreases, reaching a value of zero at a specific value of w/L that defines a bifurcation point, B (at point II in Supplementary Figure 1). For values of w/L larger than B , the beam is monostable, meaning it will return to its undeformed position ($u = 0$) if the applied force is removed. The critical value of $w/L = B$ changes as a function of θ , as represented by the orange line dividing bistable from monostable regions in Fig. 1c.

Because of this sharp critical value, only a small nudge to the geometric parameters (e.g., via active materials) is necessary to cross a bifurcation point and trigger rapid snap-through for the purpose of actuation or movement. To accomplish this, we fabricate the beams using highly anisotropic composite materials, causing anisotropic swelling of the beams upon exposure to material-specific cues (e.g., water or non-polar solvents in our initial work). As shown in Fig. 1b and c, for a beam fabricated with geometry corresponding to point I ($w/L < B$) and placed in its buckled configuration, if it were to anisotropically swell to point III ($w/L > B$) it would have to pass through the bifurcation point at point II ($w/L = B = 0.105$), above which the beam is only stable in its unbuckled configuration ($u = 0$). This forces a rapid actuation event, rapidly releasing the strain energy from the beam as it ceases to be bistable. Supplementary Movie 1 shows such an actuation event, recorded using a high-speed camera during bifurcation (in this case, PDMS-glass fiber composite beams responding to toluene). The images in Fig. 1c demonstrate the rapid actuation ($\tau < 0.01$ s) that occurs for any beam that traverses such a bifurcation point. τ represents the amount of time it takes

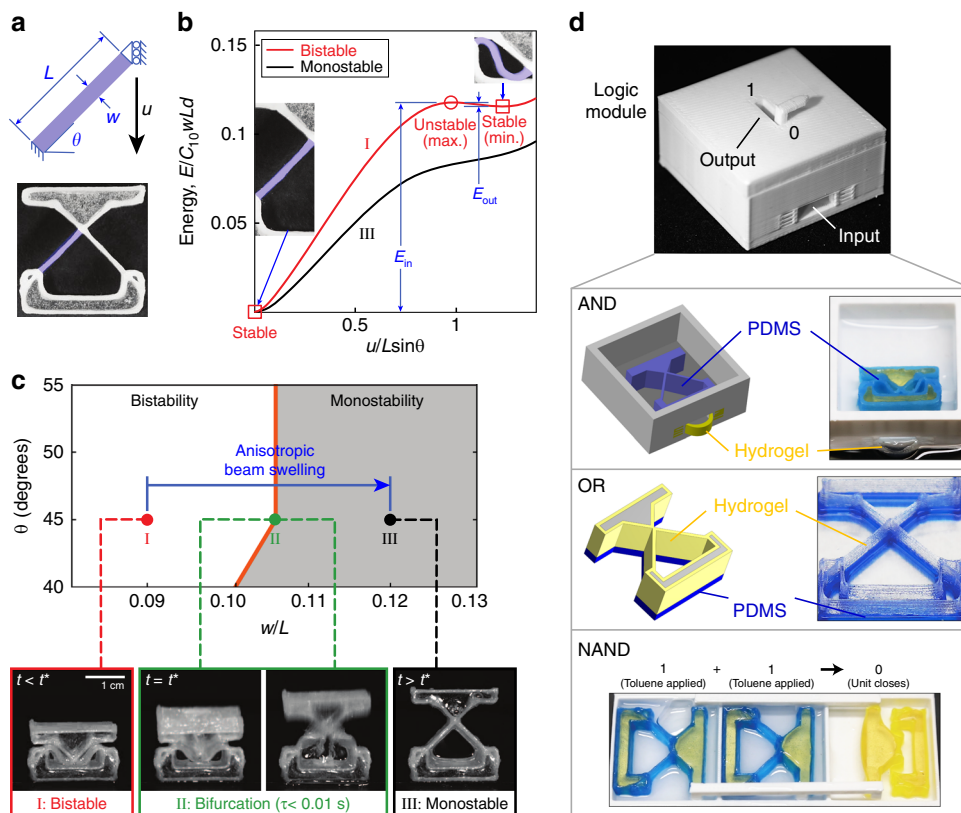


Fig. 1 Overview of bifurcation-based actuation. **a** Schematic and photo of beams, with key geometric parameters and boundary conditions. **b** The normalized strain energy, $E/(C_{10}wLd)$, where C_{10} is a material parameter in the Holzapfel-Gasser-Ogden (HGO) model⁶⁵ and d is the out-of-plane thickness of the beam; plots are included for a bistable beam (red curve, I) and a monostable beam (black curve, III) as a function of normalized displacement, $u/L\sin\theta$, obtained via finite element simulations (Supplementary Note 5). Inset: photos of the undeformed ($u = 0$) and buckled configurations, corresponding to the two stable points (energy minima) on the bistable curve; the monostable curve has only the single minimum at $u = 0$. **c** Geometric phase diagram mapping geometric parameters to mechanical behavior, with schematic overlay indicating the transition from bistable to monostable (point I to point III) due to anisotropic swelling of the beams. Also shown are representative images recorded with a high-speed camera during actuation showing a unit when it is bistable (red), at the point of bifurcation when actuation occurs (green), and monostable (black). **d** A logic module which can act as one of several types of logic gates depending on the contents of the module. An AND gate can be constructed by using a hydrogel valve and a PDMS-GF15 bistable unit (requiring both water and toluene to switch from 0 to 1). An OR gate can be constructed by fabricating a composite bistable unit from both PDMS-GF5 (blue) and hydrogel (transparent) materials (this actuates if either water or toluene is applied); a functionally-complete NAND gate can be constructed by connecting two “input” bistable units to one “output” unit. In this case, only when toluene is applied to both input units will the output unit close from 1 to 0 (i.e., $1+1\rightarrow 0$)

for the actuation event (the release of the stored strain energy) once bifurcation is reached (as observed with a high-speed camera). Note, the value of w/L would remain unchanged during swelling of an isotropic beam, and thus the bifurcation point would not be reached horizontally. (Depending on the specific architecture, isotropic swelling could still lead to the crossing of a bifurcation point via an increase in θ . However, since the monostable/bistable boundary is nearly vertical, it would typically require a larger degree of material swelling to do so.) Supplementary Movies 1–3 demonstrate the feasibility of using changes to the environment to trigger snap-through instabilities^{35,44,46,60}, as also observed in nature¹. For example, Supplementary Movie 3 shows a hopper that autonomously jumps out of the way when an undesired chemical (in this case, toluene) enters its environment. We note that this behavior occurs without discrete sensors, tethering, or mechatronic actuators: the system’s combination of composition and structure is itself the sensor, control system, and actuator. By harnessing systems of 3D printable bistable, anisotropic beam units (each of which can be independently assigned its own choice of actuation timing and its own stimulus, as described later), our bioinspired

approach allows the “embodiment” of complex control in this material-structure combination.

In Fig. 1d, we demonstrate modular embodied logic, in which a mechanical logic module can produce AND, OR, or NAND output in response to chemical inputs, depending on which structures are placed inside the module. We produce an AND gate by using a hydrogel valve and a PDMS-GF15 bistable unit inside (Supplementary Figure 2). The actuation of this inner bistable unit flips the output of the module from 0 to 1. However, to achieve this, water must be present (to make the hydrogel swell and buckle, opening the valve) as well as toluene (to trigger the actuation of the unit). We produce an OR gate by constructing a bistable unit with out-of-plane arrangements of both PDMS-GF5 (blue) and hydrogel (transparent) materials. This bistable unit can actuate when either water or toluene is applied (Supplementary Movie 4). Finally, we produce a NAND gate by connecting two units (corresponding to two inputs) and one output. The stiffness of these is tuned (via geometry) such that both inputs must actuate in order to close the output unit (i.e., $1+1\rightarrow 0$). Otherwise, the output unit remains open (Supplementary Movie 5). Since NAND is a functionally complete logic gate, in principle any

gated logic could be achieved via combinations of these. To chain the logic gates into more complex systems, the mechanical response from one gate (the output) could be used either to indicate when to perform a manual pour, or to automatically open a chamber to allow fluid movement to the next gate (e.g., the input solvents for the NAND gate could be either manually poured or introduced automatically via suitable channel design).

Materials and fabrication. In the remainder of this article, we outline how to achieve this behavior, and demonstrate utility via several use cases.

To achieve the general strategy outlined above, the ideal materials would meet the following requirements: First, each material must swell in response to a defined stimulus, e.g., water, non-polar solvents, temperature, light, etc. (in this work, we demonstrate the use of the first two of these stimuli, but any would work). Second, the materials swell *anisotropically* to alter the key geometric parameter (w/L) when exposed to their stimuli, allowing a well-controlled approach to move through a bifurcation. Third, the materials should be sufficiently elastic to maintain a buckled configuration (maximum material strain of $\epsilon_{\max} < 0.15$) without prohibitive time-dependent relaxation, as it is this stored elastic energy that enables the actuation event. Finally, the materials (or material precursors) must be patternable with high structural fidelity, since the mechanical response of the beams is determined by precise values of geometric parameters.

While 3D printers make it relatively easy to achieve sufficient structural fidelity of the beams (the fourth point above), most conventional 3D printers are unable to simultaneously achieve the other requirements⁶¹. Direct ink writing (DIW) is an extrusion-based 3D printing technique^{61,62} which offers a large degree of materials flexibility, and is ideal for producing anisotropic materials (fibers align due to material shear in the nozzle^{40,63} (Fig. 2a)). This approach allows us to meet all four

criteria above, but requires some rheological tuning of the materials to allow printing (Fig. 2b–d and Supplementary Figure 3). In this work, we make use of two materials that respond to two distinct stimuli: a PDMS-based material (containing short glass fibers to provide anisotropy), which swells in the presence of non-polar solvents, such as toluene or hexane; and a hydrogel-based matrix (containing cellulose fibrils to provide anisotropy) that swells in the presence of water. Our PDMS ink formulation (see Methods) shows the rheological properties desired for DIW, including a decrease in apparent viscosity with increasing shear rate (Fig. 2b) and a viscoelastic yielding behavior that is characterized by a high storage modulus (G') when the shear stress is low (allowing the material to maintain its shape and to behave like an elastic solid) and a defined yield stress above which the storage modulus suddenly drops (allowing flowability through the nozzle) (Fig. 2c). A similar rheological profile is observed for the hydrogel material (Supplementary Figure 3). Because of the alignment of the fibers during extrusion (Fig. 2d), a high degree of mechanical anisotropy can be achieved. We characterize this by printing tensile specimens with fiber alignment both parallel with (“Longitudinal”) and perpendicular to (“Transverse”) the loading direction, subsequently testing these under quasistatic tension (see Methods) (Fig. 2e). Since the glass fibers are much shorter than the beam length, the Halpin–Tsai model⁶⁴ is used, with the best fit corresponding to a matrix stiffness of $E_m = 2.96$ MPa and a fiber stiffness of $E_f = 52.13$ GPa (details in Supplementary Note 3). With increasing glass fiber volume fraction, the longitudinal stiffness, E_L , increases much more than the transverse value, E_T (Fig. 2e), as expected for short fiber composites. With 15 vol% glass fibers, significant mechanical anisotropy ($E_L/E_T = 10.8$) is obtained while good printability is maintained. Additional tensile tests on swollen samples and stress relaxation tests are shown in Supplementary Figure 4.

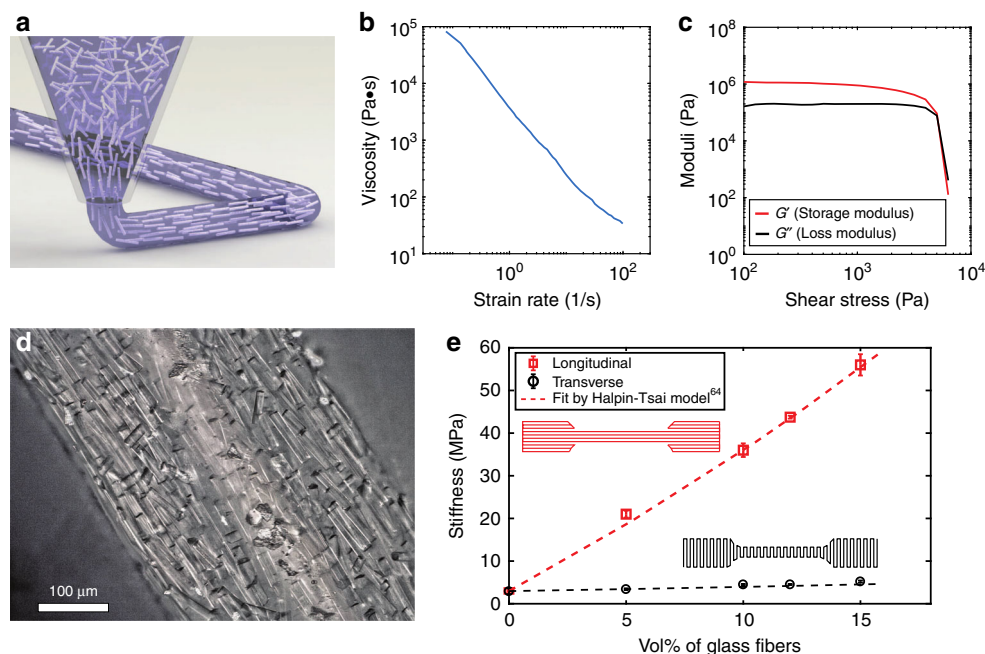


Fig. 2 Direct ink writing (DIW) of PDMS-glass fiber composites. **a** Schematic of extrusion of PDMS ink during DIW 3D printing, leading to alignment of glass fibers. **b, c** Rheological characterization of the PDMS-GF ink shows shear-thinning and yield-stress behavior, respectively. **d** An optical micrograph showing material printed using PDMS-GF ink (15 vol% glass fibers), with alignment of glass fibers along the print direction. **e** Stiffness of PDMS-GF composites (after curing of printed structures) as a function of the volume fraction of glass fibers and the fiber orientation, based on tensile testing of printed specimens (“Longitudinal” and “Transverse” indicate printing and fiber orientation that is parallel with or perpendicular to the loading direction, respectively), and fit using the Halpin–Tsai model⁶⁴

Mechanical behavior. In prior work on the bistability of laterally-constrained beams⁵¹, the relationship between beam geometry (the two key geometric parameters θ and w/L) and the stability behavior (e.g., bistable or monostable) was considered material-independent. However, this conclusion implicitly assumed that the material was isotropic. In fact, the degree of material anisotropy is also essential for determining the stability. Using experiments and finite element analysis (FEA), we locate the boundary between regions of monostability and bistability in the geometric phase diagram (e.g., Fig. 1c) for the more general case, in which the material anisotropy is allowed to vary. We first fit an anisotropic hyperelastic mechanical model, the Holzapfel–Gasser–Ogden (HGO) model⁶⁵, to our experimental tensile data for the case of 15 vol% glass fibers (Supplementary Figure 5a) and then use this to conduct a parametric study (Fig. 3). The results (Fig. 3a, b) indicate that a beam with $\theta = 45^\circ$ is bistable if w/L is less than 0.105 (i.e., the second energy well exists, and therefore the quantity E_{out} can be defined and is nonzero), and monostable otherwise (Supplementary Note 5). This is consistent with our experimentally-determined phase boundary between $0.102 < w/L < 0.108$ (Supplementary Note 4). We develop a more complete phase diagram by systematically varying θ and w/L and determining the normalized energy barrier $E_{out}/(C_{10}wLd)$ (Fig. 3c), which is very different from the isotropic case⁵¹. As discussed more in Supplementary Note 5, the phase boundary depends strongly on the degree of anisotropy (see Fig. 3d and Supplementary Figure 5c, with $k_1 = 0$ indicating isotropy and increasing k_1 indicating increasing anisotropy). For a beam of fixed length, L , the greater the degree of material anisotropy, the thinner the beam must be to be bistable (Supplementary Note 5).

The anisotropy in stiffness imparted by the alignment of the glass fibers produces anisotropic swelling when the material is exposed to a suitable solvent (Fig. 4). To characterize this, we measured L and w of the printed beams during exposure to the solvent under an optical microscope. Since PDMS swells strongly in non-polar solvents, we used toluene as the stimulus⁶⁶. When allowed to become fully saturated by toluene (at time $t = t_s$), the isotropic PDMS matrix (no glass fibers) swells until each linear dimension has increased by 42%, corresponding to a swelling ratio of $\eta = 1.42$ (see Fig. 4a and Supplementary Note 6). The mechanical anisotropy produced by aligned fibers (e.g., in PDMS-GF composites) significantly reduces the swelling ratio in the direction of fiber alignment (longitudinal direction), $\eta_L = L_s/L_0$. The magnitude of this reduction increases as the volume fraction of the fibers (and concomitantly the degree of anisotropy) increases. In contrast, there is only a slight reduction in the swelling ratio in the direction perpendicular to the fibers (the transverse swelling ratio, $\eta_T = w_s/w_0$) relative to the isotropic case (see Fig. 4a), since the fibers do not provide significant reinforcement perpendicular to their alignment. The swelling anisotropy (defined as η_T/η_L) therefore increases with increasing fiber volume fraction (Fig. 4b). Accordingly, w will increase more than L upon exposure to a solvent, and the key geometric parameter w/L that defines the nonlinear behavior of the beam can be altered merely by exposing it to a suitable solvent. The swelling anisotropy (η_T/η_L) also determines the range in parameter space, $\Delta w/L$, through which the geometry of a beam is able to move based on such swelling. The choice of the initial beam geometry w_0/L_0 at fabrication determines whether this range is sufficient to bring the beam’s geometry through the bifurcation (i.e., the $k_1 = 10$ phase boundary in Fig. 3d for our 15

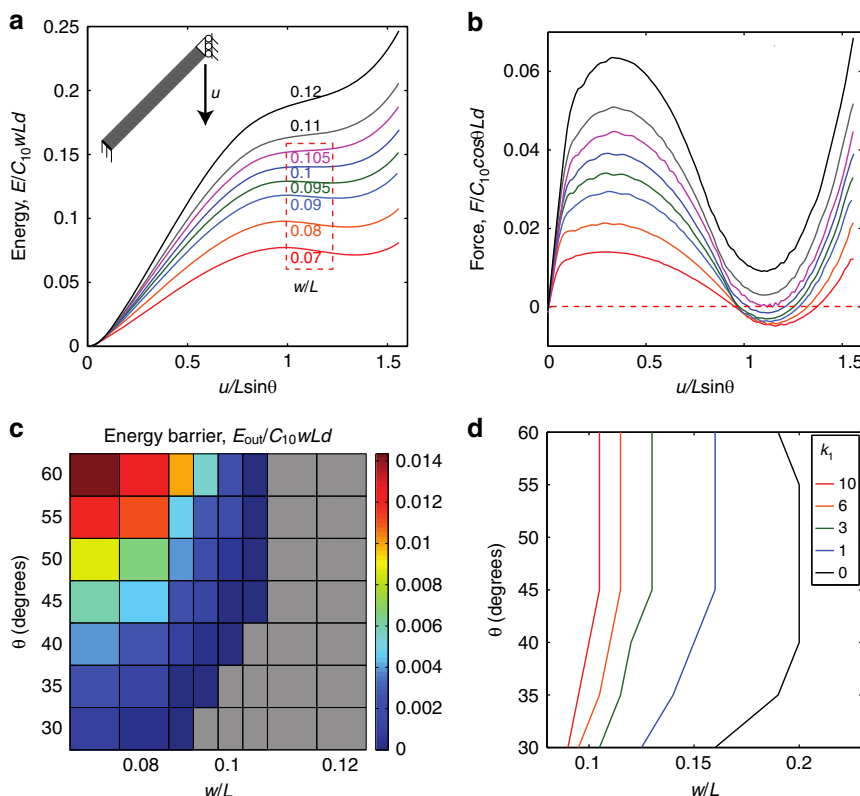


Fig. 3 Finite element analysis to determine the phase boundary for anisotropic materials. **a, b** Energy and force, respectively, as a function of displacement, for a beam with $\theta = 45^\circ$ and a w/L ratio varying from 0.07 to 0.12. The dashed box indicates bistable w/L values. **c** Energy barrier, E_{out} , necessary for a buckled beam to snap back to its undeformed configuration (the gray region indicates that the beam is monostable). **d** The phase boundaries as a function of anisotropy, where $k_1=0$ indicates an isotropic material and increasing k_1 indicates increasing anisotropy (i.e., larger stiffness ratio E_L/E_T); everything to the left of a particular line is bistable for that value of k_1

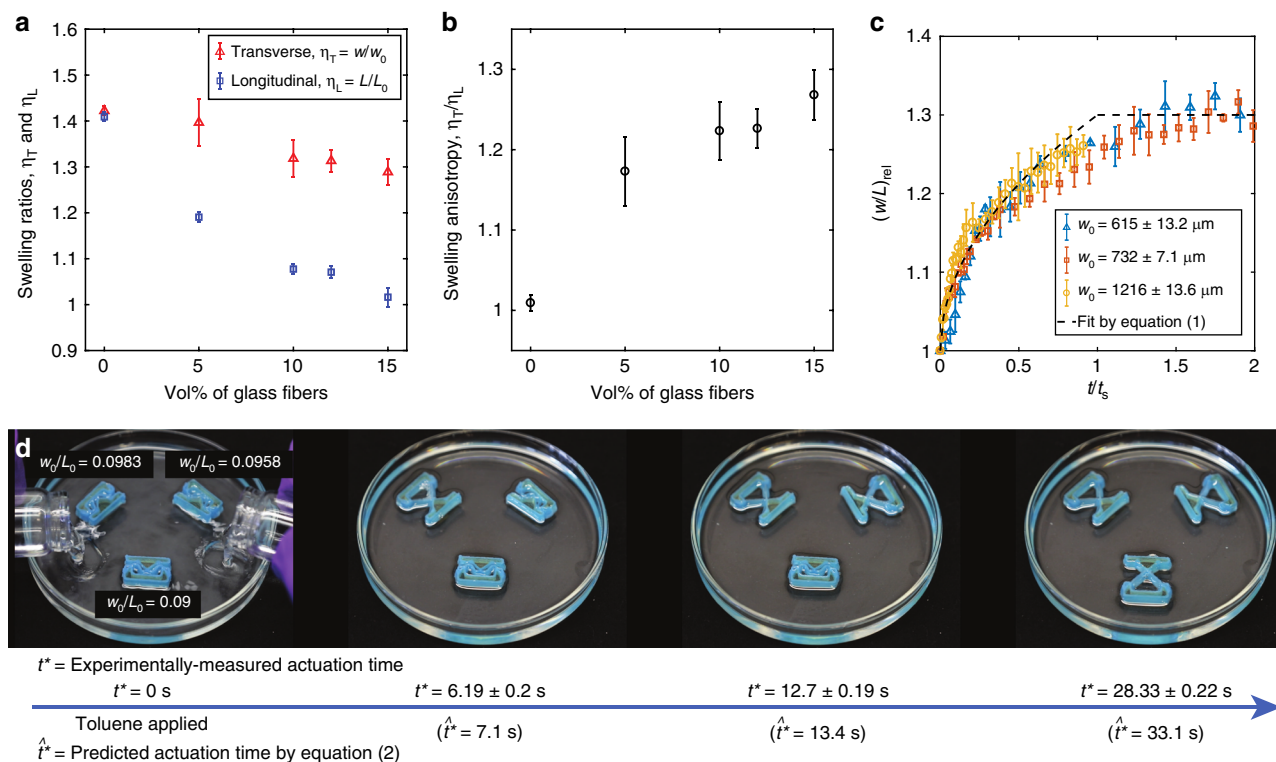


Fig. 4 Control of actuation time. **a** Swelling ratio in the transverse ($\eta_T = w/w_0$) and longitudinal ($\eta_L = L/L_0$) directions for PDMS–GF composite materials after submersion in toluene for one day. **b** Swelling anisotropy, η_T/η_L as a function of volume fraction of glass fibers. **c** The relative slenderness ratio $(w/L)_{rel}$ as a function of time for beams with different initial widths (time is normalized by saturation time, t_s , to account for the dependence of diffusion time on volume of material). **d** Actuation time can be controlled by selecting specific values for the initial beam geometry, w_0/L_0 . The measured time t^* is given, as well as the predicted time, \hat{t}^* , as calculated from equation (2). The error bars are the standard deviations computed from multiple measurements

vol% PDMS–GF), as necessary to trigger an actuation event (Fig. 1c). As a proof of concept, we provide simple demonstrations of such autonomous actuation in Supplementary Movies 2 and 6 for material printed from PDMS–GF and exposed to toluene. In Supplementary Movie 2, a bistable unit actuates and jumps dramatically due to the rapid release of strain energy from the buckled beams. In Supplementary Movie 6, a bistable unit is integrated with the lid of a 3D printed box, and the strain energy is harnessed to open the lid when an appropriate solvent is encountered. In this case, the box remains closed when placed in water, but when the water becomes contaminated by the addition of toluene, the beams actuate and open the box lid. Using this approach, for example, a box could float indefinitely in the ocean and wait to autonomously open to release a chemical or to obtain a sample when a particular pollutant is encountered, without using batteries or sensors.

Controlling the time of actuation. The distance between w_0/L_0 and the bifurcation B will set a time interval between the introduction of the stimulus ($t = 0$) and the time at which the beam actuates ($t = t^*$). To quantify this time, we measured the changing value of w/L during solvent swelling (Fig. 4c) for the PDMS–GF15 ink during submersion in toluene. We normalize the beam’s changing w/L ratio (see also Supplementary Figure 6 for non-normalized data) by the initial ratio w_0/L_0 to provide a relative value, $(w/L)_{rel} = (w/L)/(w_0/L_0)$, which, assuming simple diffusion, can be derived (Supplementary Note 7) as

$$(w/L)_{rel} = \begin{cases} 1 + \sqrt{(t/t_s)}(\eta_T - 1) & , t < t_s \\ \eta_T & , t \geq t_s \end{cases} \quad (1)$$

where the time $t_s = w_0^2/8D$ is the time we expect the beam to be saturated (based on diffusion), and D is the diffusion coefficient of toluene in PDMS. Using equation (1) (Supplementary Note 7), the time at which we expect the beam geometry w/L to reach the bifurcation point B (and hence to actuate) is

$$\hat{t}^* = \frac{(BL_0 - w_0)^2}{8D(\eta_T - 1)^2} \quad (2)$$

(note, we use \hat{t}^* to indicate the time of actuation predicted by equation (2), and t^* to indicate the measured time). Fig. 4d and Supplementary Movie 7 demonstrate how different w_0/L_0 values produce different t^* in accordance with equation (2). We have printed samples with widths of 600–850 μm and lengths of 7–9 mm. The actuation time for these can range from about 0.6 s to 108 s, which almost spans the range of theoretically predicted times (0–130 s) by equation (2).

Since B and η_T are unitless and D is an intrinsic parameter, the maximum actuation time for a beam with slenderness ratio w_0/L_0 would scale like w_0^2 . For example, if the beams were made an order of magnitude smaller (e.g., around 85 μm in width) the range of available actuation times would decrease from roughly 0–130 s to 0–1.3 s. For any length scale, the theoretical upper bound of the actuation time is the time to saturation, $t_s = w_0^2/8D$, and the theoretical lower bound can be arbitrarily close to zero, as w_0/L_0 can always be chosen to satisfy $B - w_0/L_0 \rightarrow 0$. In reality, small perturbations in environmental conditions and fabrication limitations in beam geometry make infinitesimal \hat{t}^* unachievable and increase the uncertainty in experimental actuation time at these smaller values.

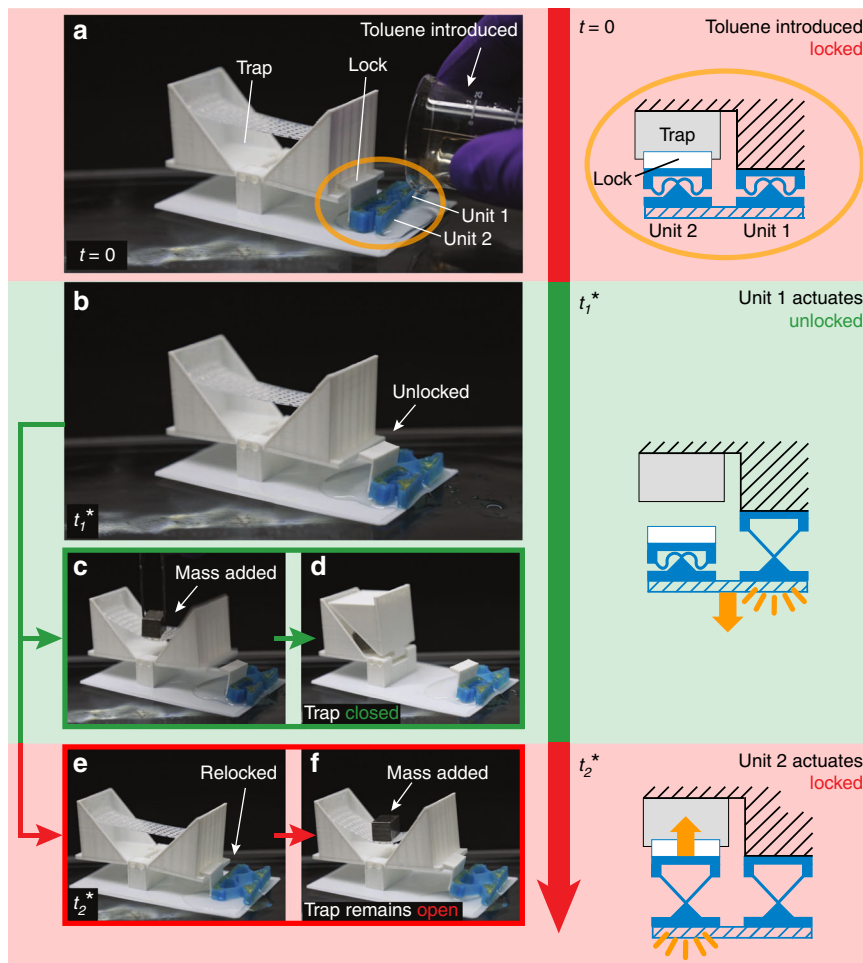


Fig. 5 A “flytrap” with embodied logic **Close**($S_{\text{toluene}}, S_{\text{mass}} \mid t_{\text{mass}}^* - t_1^* < t_2^* - t_1^*$). **a** Toluene is applied to a flytrap-inspired system which is prevented from closing by a lock that is toggled by two actuating units. **b** The unit with larger w_0/L_0 actuates first (at time t_1^*), which unlocks the lobe. **c, d** If a mechanical load is applied while the flytrap is unlocked it closes. **e, f** Later, the second bistable unit actuates (at time t_2^*) and relocks the lobe; adding a mechanical load at this point has no effect

Despite the simplistic assumptions in the model, we found that the average discrepancy between \hat{t}^* and t^* was about 17% for samples designed to actuate more than 20 s after exposure to the stimulus. As this time is reduced, the relative error of the model increases. For example, for samples designed to actuate at times less than 5 s after exposure to the stimulus, the relative error of the model increases to about 44%. The high discrepancy for short actuation times (<5 s) arises from several challenging factors: non-uniform exposure to the chemical stimulus (not accounted for in the model, which assumes instantaneous, uniform exposure); the particularly close proximity of the geometric parameters to a bifurcation point when short delay times are desired, corresponding to a very small energy barrier; experimental uncertainty in the precise location of the phase boundary (exacerbated by the small energy barrier near bifurcation); and deviations in friction between the material and the substrate. At longer intervals of time (>5 s) these problems are diminished. In practice, this uncertainty would set a practical limit on how closely a sequence of ordered actuation events could be temporally spaced.

If we allow time for the solvent to evaporate, the beams return to their initial geometric parameters (w_0/L_0), and are once again bistable (see Supplementary Figure 7, and Supplementary Table 1). External energy is required to reset the units to the higher-energy state in order to reuse them. At ambient conditions, the drying time is about 70 min (though this could

be smaller or larger depending on the length scale of the system) after which the units can be reset to the higher-energy state by compression (to buckle the beams again). We performed repeated tests (actuation–drying–resetting–actuation) on five units and found that the intra-sample variability of actuation time is comparable with the inter-sample variability, as discussed above (see Supplementary Table 2).

Demonstrations of embodied logic. In addition to the control of actuation time, self-actuating systems that consist of multiple actuating units (each of which may be a different material, to respond to different stimuli) can be constructed. There are many ways that these can be arranged, leading to different possible system functions of varying complexity. We utilize a shorthand to describe some of these possible functions: first, we indicate a functional event in bold followed in parentheses by the condition that is necessary for that event to occur; example functions include **Open** and **Close**, referring, e.g., to the opening or closing of a box. Second, the application of a stimulus is indicated by the symbol S with an appropriate subscript; here, stimuli can include S_{toluene} (which actuates PDMS-based materials), S_{water} (which actuates hydrogel-based materials), and S_{mass} (which refers to placing a mass on the structure). For example, **Open**(S_{water}) would indicate that a structure should open when exposed to water, which would be accomplished by using a hydrogel-based

material to actuate. Finally, if multiple stimuli must occur within some time interval, this is indicated by a value assigned to Δt^* . As a first example, we 3D print a box (see Methods) which is designed to autonomously open when exposed to toluene, but then to close again after a defined interval of time (e.g., 20 s). This behavior can be written as **TimedOpen**($S_{\text{toluene}} \mid \Delta t^* = 20 \text{ s}$). To open and then close the box, we need two actuation events, which we accomplish by integrating two PDMS-GF actuating units with the box, each with different values of w_0/L_0 . These values are chosen such that simultaneous exposure to toluene will cause them to reach the phase boundary, B , 20 s apart. We show this behavior in Supplementary Movie 8: after exposure to toluene, the right unit actuates first, opening the box. Then, after $\sim 20 \text{ s}$, the left unit actuates and closes the box. The second demonstration mimics the rapid closing of the Venus flytrap when an object (denoted S_{mass}) is placed on a waiting ledge, with the added requirement that the trap is only in operation if a chemical signal (toluene) has been applied (see Supplementary Movie 9). We can represent this behavior as **Close**($S_{\text{toluene}} \wedge S_{\text{mass}}$). The trap is locked until a PDMS-based unit actuates, preventing the lobes from closing until $t \geq t^*$ even if a load is applied before then.

Figure 5 shows a similar Venus flytrap-inspired example, but with more complex control logic. In this example, there are two actuating units made from PDMS-GF, which are designed to actuate 10 s apart (Fig. 5a). The first of these (which actuates at t_1^*) activates the system by removing the lock (as in Fig. 5b) while the second (which actuates at t_2^*) re-locks the flytrap, once again preventing it from closing. If a mass is placed on a platform in the center of the flytrap at a time between t_1^* and t_2^* (i.e., when the lock is disengaged) the lobes will close (Fig. 5c, d and Supplementary Movie 10). If the mass is placed on the platform when the lock is engaged (e.g., after t_2^* , as in Fig. 5e, f and Supplementary Movie 11) it will have no effect. This functionality is described by **Close**($S_{\text{toluene}}, S_{\text{mass}} \mid t_{\text{mass}} - t_1^* < t_2^* - t_1^*$), where the comma indicates an ordered list of stimuli, and $t_2^* - t_1^* = 10 \text{ s}$.

Finally in Fig. 6, we demonstrate a multi-stimuli-responsive system^{67,68}, which uses two materials that respond to two orthogonal stimuli (i.e., hydrogel, which responds to water, and PDMS, which responds to a non-polar solvent such as toluene). We compose a box which follows the behavior **Open**($S_{\text{water}} \wedge S_{\text{toluene}} \mid t_{\text{hydrogel}}^* < t_{\text{PDMS}}^*$), as shown in Fig. 6a. Application of S_{water} causes the hydrogel-based unit to actuate, opening a lock (at time t_{hydrogel}^*) that otherwise obstructs the opening of the lid. Application of S_{toluene} causes the PDMS-based unit to actuate (at time t_{PDMS}^*), pushing open the lid if it has been unlocked (Fig. 6b, c and Supplementary Movie 12). If instead we apply only toluene, the hydrogel-based lock does not respond, and the box remains closed even when the PDMS-based unit pushes on the lid (Fig. 6d, e and Supplementary Movie 13). This capability could be used, for example, to produce a sampling box that autonomously opens when it encounters an oil–water interface, without any external power or solid-state sensors and actuators.

These principles can be further extended to 2D or 3D by designing more complicated arrangements of beams. As a demonstration of this, we manufactured 2D samples using PDMS-based materials and illustrated autonomous deployment due to the presence of toluene (Supplementary Movie 14).

Discussion

In summary, we have designed and 3D printed systems of self-actuating structures capable of simple logic (AND, OR, and NAND) and controlled timing of actuation in response to multiple stimuli. We have accomplished this using PDMS-based and hydrogel-based materials that respond to different environmental stimuli. Due to the use of short fiber composites and the

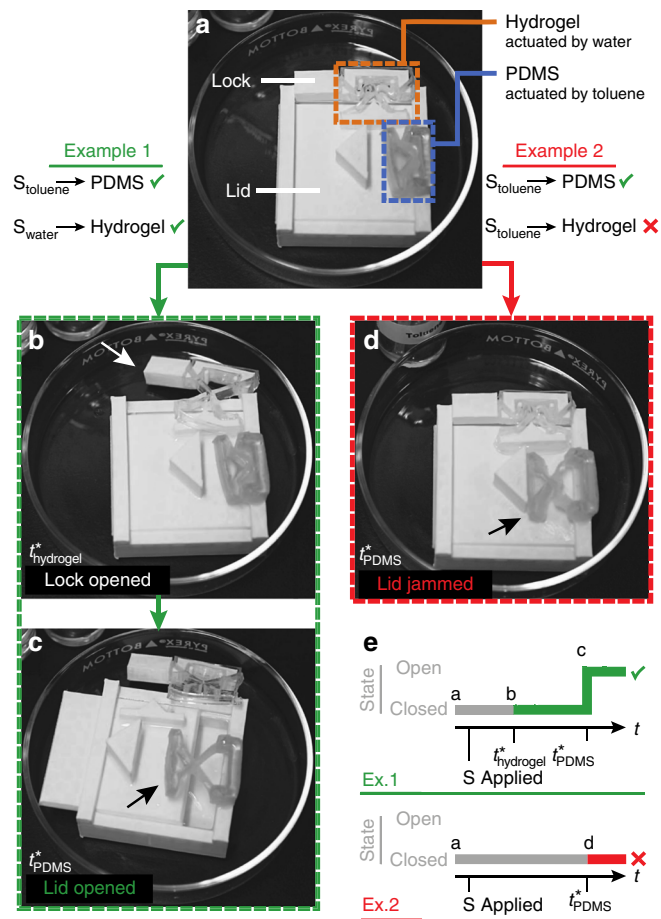


Fig. 6 Multimaterial responsive systems, e.g., **Open**($S_{\text{water}} \wedge S_{\text{toluene}} \mid t_{\text{hydrogel}}^* < t_{\text{PDMS}}^*$). **a** A box with a lid which is unlocked upon actuation of a hydrogel-based unit (at time t_{hydrogel}^*) and subsequently opened upon actuation of a PDMS-based unit (at time t_{PDMS}^*). **b, c** Example 1: if water is applied to the hydrogel-based unit and toluene to the PDMS-based unit, the lid is unlocked and then pushed open, successfully opening the box (Supplementary Movie 12). **d** Example 2: if toluene is applied to both units, the PDMS-based unit actuates as it should, but because the hydrogel-based unit is unresponsive to toluene, the lock interferes and the lid remains closed (Supplementary Movie 13). **e** Diagram representing the system logic and the behaviors of the system in Examples 1 and 2

alignment of the fibers during extrusion, the beams swell anisotropically in the presence of suitable stimuli, triggering rapid and large-amplitude configuration changes at predetermined times (as the geometric parameter w_0/L_0 passes a bifurcation point). Using solely architected soft materials as self-actuating functional elements, our approach enables complex function and control of timing in response to multiple stimuli. We demonstrated several autonomous responsive systems in this work as examples of our approach, all performing their designated functions without mechatronics, traditional control systems, or tethering. This includes a hopper that autonomously jumps when an undesired chemical is introduced, a “flytrap” that only closes if mechanically stimulated during a pre-programmed interval of time, and a box that only opens if it encounters both non-polar solvents and water. While this work focuses on the autonomous release of strain energy to produce precise actuation events, these concepts could be integrated with more complex systems. For example, advances from soft robotics, such as the integration of pneumatic or chemical energy sources⁶⁹, could allow the units to be autonomously reset to allow repeated actuation events. We also

note that the nonlinear behavior of the beams (e.g., the location of the bifurcation points in parameter space) is scale-independent, and therefore the systems have the potential to be scaled down or up as may be necessary for additional applications, e.g., in soft robotics, biomedical devices, and deployable structures. Finally, we made use of materials that respond to non-polar solvents or to water, but the same concept would apply to matrices that respond to other cues (e.g., light, temperature, and electric potential) as long as the printed materials are anisotropic.

Methods

Ink preparation and 3D printing. PDMS and glass fibers are mixed under vacuum, and then transferred to a syringe and centrifuged (see more discussion in Supplementary Information). We use nozzles with an inner diameter of 410- μm for PDMS-based ink printing in this work. The hydrogel has an N-isopropylacrylamide (NIPAm) network and nanofibrillated cellulose (NFC) as a filler. After preparation of the ink (discussion in Supplementary Information), it is printed through a nozzle of diameter 250- μm . To improve the bistable response, two parallel filaments of the hydrogel-based ink are printed and then PDMS is injected in between to form a hydrogel beam. A 3D translation stage controls motion of the nozzle during printing. The PDMS-based ink is thermally cured and epoxy is cast and cured to provide desired boundary conditions. The hydrogel-based ink is cured by UV cross-linking and then mounted on 3D printed polylactic acid (PLA) pieces. We used fused deposition modeling (FDM) for fabrication of parts for demonstrations, with the functional PDMS or hydrogel units integrated with these by hand. The parts are fabricated on a MakerGear M2. We use a nozzle of diameter 0.25 mm at an extrusion temperature of 190 °C, a bed temperature of 65 °C, and speeds of 30–80 mm/s.

Mechanical testing. We performed tensile tests on an Instron Model 5564 (displacement control), with tensile bars printed in either longitudinal or transverse directions relative to the loading direction. The nominal strain rate is constant at 1% for all tests. The actuation time associated with the snap-through of the structures was measured using a high-speed camera (Photron AX200) at 2000 frames per second. We performed continuous shear-rate ramp and stress sweep rheology tests on a rheometer (TA Instruments® AR2000) at ambient temperature using a 20-mm parallel plate with a 140- μm gap size for both PDMS-GF and hydrogel-based inks.

Data availability

All data generated or analysed during this study are included in this published article (and its supplementary information files).

Received: 18 June 2018 Accepted: 12 December 2018

Published online: 10 January 2019

References

1. Skotheim, J. M. Physical limits and design principles for plant and fungal movements. *Science* **308**, 1308–1310 (2005).
2. Burgert, I. & Fratzl, P. Actuation systems in plants as prototypes for bioinspired devices. *Philos. Trans. R. Soc. A Math. Phys. Eng. Sci.* **367**, 1541–1557 (2009).
3. Elbaum, R., Zaltzman, L., Burgert, I. & Fratzl, P. The role of wheat awns in the seed dispersal unit. *Science* **316**, 884–886 (2007).
4. Reyssat, E. & Mahadevan, L. Hygromorphs: from pine cones to biomimetic bilayers. *J. R. Soc. Interface* **6**, 951–957 (2009).
5. Rafsanjani, A., Brulé, V., Western, T. L. & Pasini, D. Hydro-responsive curling of the resurrection plant *Selaginella lepidophylla*. *Sci. Rep.* **5**, 8064 (2015).
6. Forterre, Y., Skotheim, J. M., Dumais, J. & Mahadevan, L. How the Venus flytrap snaps. *Nature* **433**, 421–425 (2005).
7. Volkov, A. G., Adesina, T., Markin, V. S. & Jovanov, E. Kinetics and mechanism of *Dionaea muscipula* trap closing. *Plant Physiol.* **146**, 694–702 (2007).
8. Yang, R., Lenaghan, S. C., Zhang, M. & Xia, L. A mathematical model on the closing and opening mechanism for Venus flytrap. *Plant Signal. Behav.* **5**, 968–978 (2010).
9. Wehner, M. et al. An integrated design and fabrication strategy for entirely soft, autonomous robots. *Nature* **536**, 451–455 (2016).
10. Leong, T. G. et al. Therless thermobiochemically actuated microgrippers. *Proc. Natl Acad. Sci.* **106**, 703–708 (2009).
11. Jin, B. et al. Programming a crystalline shape memory polymer network with thermo- and photo-reversible bonds toward a single-component soft robot. *Sci. Adv.* **4**, eaao3865 (2018).
12. Wani, O. M., Zeng, H. & Priimagi, A. A light-driven artificial flytrap. *Nat. Commun.* **8**, 15546 (2017).
13. Fernandes, R. & Gracias, D. H. Self-folding polymeric containers for encapsulation and delivery of drugs. *Adv. Drug Deliv. Rev.* **64**, 1579–1589 (2012).
14. Shim, T. S., Kim, S. H., Heo, C. J., Jeon, H. C. & Yang, S. M. Controlled origami folding of hydrogel bilayers with sustained reversibility for robust microcarriers. *Angew. Chemie - Int. Ed.* **51**, (1420–1423 (2012).
15. Hines, L., Petersen, K., Lum, G. Z. & Sitti, M. Soft actuators for small-scale robotics. *Adv. Mater.* **29**, 1603483 (2017).
16. Jeon, S. J., Hauser, A. W. & Hayward, R. C. Shape-morphing materials from stimuli-responsive hydrogel hybrids. *Acc. Chem. Res.* **50**, 161–169 (2017).
17. Studart, A. R. & Erb, R. M. Bioinspired materials that self-shape through programmed microstructures. *Soft Matter* **10**, 1284–1294 (2014).
18. White, T. J. & Broer, D. J. Programmable and adaptive mechanics with liquid crystal polymer networks and elastomers. *Nat. Mater.* **14**, 1087–1098 (2015).
19. Zeng, H., Wasylczyk, P., Wiersma, D. S. & Priimagi, A. Light robots: bridging the gap between microrobotics and photomechanics in soft materials. *Adv. Mater.* **30**, 1703554 (2017).
20. Ko, H. & Javey, A. Smart actuators and adhesives for reconfigurable matter. *Acc. Chem. Res.* **50**, 691–702 (2017).
21. Stuart, M. A. C. et al. Emerging applications of stimuli-responsive polymer materials. *Nat. Mater.* **9**, 101–113 (2010).
22. Yan, X., Wang, F., Zheng, B. & Huang, F. Stimuli-responsive supramolecular polymeric materials. *Chem. Soc. Rev.* **41**, 5869–6216 (2012).
23. Momeni, F., Mehdi Hassani, N., S., Liu, X. & Ni, J. A review of 4D printing. *Mater. Des.* **122**, 42–79 (2017).
24. Boothby, J. M., Kim, H. & Ware, T. H. Shape changes in chemoresponsive liquid crystal elastomers. *Sens. Actuators B Chem.* **240**, 511–518 (2017).
25. Ge, Q., Qi, H. J. & Dunn, M. L. Active materials by four-dimension printing. *Appl. Phys. Lett.* **103**, 131901 (2013).
26. Na, J. H. et al. Programming reversibly self-folding origami with micropatterned photo-crosslinkable polymer trilayers. *Adv. Mater.* **27**, 79–85 (2015).
27. Liu, K., Wu, J., Paulino, G. H. & Qi, H. Programmable deployment of tensegrity structures by stimulus-responsive polymers. *Sci. Rep.* **7**, 3511 (2017).
28. Bakarich, S. E., Gorkin, R., Panhuis, M., Het. In & Spinks, G. M. 4D printing with mechanically robust, thermally actuating hydrogels. *Macromol. Rapid Commun.* **36**, 1211–1217 (2015).
29. Ambulo, C. P. et al. Four-dimensional printing of liquid crystal elastomers. *ACS Appl. Mater. Interfaces* **9**, 37332–37339 (2017).
30. López-Valdeolivas, M., Liu, D., Broer, D. J. & Sánchez-Somolinos, C. 4D printed actuators with soft-robotic functions. *Macromol. Rapid Commun.* **39**, 1700710 (2017).
31. Kotikian, A., Truby, R. L., Boley, J. W., White, T. J. & Lewis, J. A. 3D printing of liquid crystal elastomeric actuators with spatially programmed nematic order. *Adv. Mater.* **30**, 1706164 (2018).
32. Oosten, C. L. Van, Bastiaansen, C. W. M. & Broer, D. J. Printed artificial cilia from liquid-crystal network actuators modularly driven by light. *Nat. Mater.* **8**, 677–682 (2009).
33. Zeng, H., Wani, O. M., Wasylczyk, P., Kaczmarek, R. & Priimagi, A. Self-regulating iris based on light-actuated liquid crystal elastomer. *Adv. Mater.* **29**, 1701814 (2017).
34. Rogó, M., Zeng, H., Xuan, C., Wiersma, D. S. & Wasylczyk, P. Light-driven soft robot mimics caterpillar locomotion in natural scale. *Adv. Opt. Mater.* **4**, 1689–1694 (2016).
35. Shankar, M. R. et al. Contactless, photoinitiated snap-through in azobenzene-functionalized polymers. *Proc. Natl Acad. Sci.* **110**, 18792–18797 (2013).
36. Hubbard, A. M., Mailen, R. W., Zikry, M. A., Dickey, M. D. & Genzer, J. Controllable curvature from planar polymer sheets in response to light. *Soft Matter* **13**, 2299–2308 (2017).
37. Tavakol, B. & Holmes, D. P. Voltage-induced buckling of dielectric films using fluid electrodes. *Appl. Phys. Lett.* **108**, 112901 (2016).
38. Pelrine, R., Kornbluh, R., Pei, Q. & Joseph, J. High-speed electrically actuated elastomers with strain greater than 100%. *Science* **287**, 836–840 (2000).
39. Cao, J. et al. Untethered soft robot capable of stable locomotion using soft electrostatic actuators. *Extrem. Mech. Lett.* **21**, 9–16 (2018).
40. Gladman, A. S., Matsumoto, E. A., Nuzzo, R. G., Mahadevan, L. & Lewis, J. A. Biomimetic 4D printing. *Nat. Mater.* **15**, 413–418 (2016).
41. Raviv, D. et al. Active printed materials for complex self-evolving deformations. *Sci. Rep.* **4**, 7422 (2014).
42. Stoychev, G., Guiducci, L., Turcaud, S., Dunlop, J. W. C. & Ionov, L. Hole-programmed superfast multistep folding of hydrogel bilayers. *Adv. Funct. Mater.* **26**, 7733–7739 (2016).

43. Wu, J. et al. Multi-shape active composites by 3D printing of digital shape memory polymers. *Sci. Rep.* **6**, 24224 (2016).
44. Chen, T., Bilal, O. R., Shea, K. & Daraio, C. Harnessing bistability for directional propulsion of soft, untethered robots. *Proc. Natl Acad. Sci.* **115**, 5698–5702 (2018).
45. Zhang, X. et al. Optically- and thermally-responsive programmable materials based on carbon nanotube-hydrogel polymer composites. *Nano. Lett.* **11**, 3239–3244 (2011).
46. Abdullah, A. M., Braun, P. V. & Hsia, K. J. Programmable shape transformation of elastic spherical domes. *Soft Matter* **12**, 6184–6195 (2016).
47. Boothby, J. M. & Ware, T. H. Dual-responsive, shape-switching bilayers enabled by liquid crystal elastomers. *Soft Matter* **13**, 4349–4356 (2017).
48. Hu, N. & Burgueño, R. Buckling-induced smart applications: recent advances and trends. *Smart Mater. Struct.* **24**, 63001 (2015).
49. Bertoldi, K., Vitelli, V., Christensen, J. & Van Hecke, M. Flexible mechanical metamaterials. *Nat. Rev. Mater.* **2**, 17066 (2017).
50. Kochmann, D. & Bertoldi, K. Exploiting microstructural instabilities in solids and structures: from metamaterials to structural transitions. *Appl. Mech. Rev.* **69**, 050801 (2017).
51. Shan, S. et al. Multistable architected materials for trapping elastic strain energy. *Adv. Mater.* **27**, 4296–4301 (2015).
52. Restrepo, D., Mankame, N. D. & Zavattieri, P. D. Phase transforming cellular materials. *Extrem. Mech. Lett.* **4**, 52–60 (2015).
53. Correa, D. M., Seepersad, C. C. & Haberman, M. R. Mechanical design of negative stiffness honeycomb materials. *Integr. Mater. Manuf. Innov.* **4**, 10 (2015).
54. Wang, P., Casadei, F., Shan, S., Weaver, J. C. & Bertoldi, K. Harnessing buckling to design tunable locally resonant acoustic metamaterials. *Phys. Rev. Lett.* **113**, 14301 (2014).
55. Kang, S. H. et al. Complex ordered patterns in mechanical instability induced geometrically frustrated triangular cellular structures. *Phys. Rev. Lett.* **112**, 1–5 (2014).
56. Raney, J. R. et al. Stable propagation of mechanical signals in soft media using stored elastic energy. *Proc. Natl Acad. Sci.* **113**, 9722–9727 (2016).
57. Lee, H., Xia, C. & Fang, N. X. First jump of microgel; actuation speed enhancement by elastic instability. *Soft Matter* **6**, 4342–4345 (2010).
58. Yang, X. et al. Bio-Inspired fast actuation by mechanical instability of thermoresponding hydrogel structures. *J. Appl. Mech.* **83**, 71005 (2018).
59. Che, K., Yuan, C., Wu, J., Jerry Qi, H. & Meaud, J. Three-dimensional-printed multistable mechanical metamaterials with a deterministic deformation sequence. *J. Appl. Mech.* **84**, 11004 (2016).
60. Lee, H., Zhang, J., Jiang, H. & Fang, N. X. Prescribed pattern transformation in swelling gel tubes by elastic instability. *Phys. Rev. Lett.* **108**, 214304 (2012).
61. Raney, J. R. & Lewis, J. A. Printing mesoscale architectures. *Mrs. Bull.* **40**, 943–950 (2015).
62. Lewis, J. A. Direct ink writing of 3D functional materials. *Adv. Funct. Mater.* **16**, 2193–2204 (2006).
63. Compton, B. G. & Lewis, J. A. 3D-printing of lightweight cellular composites. *Adv. Mater.* **26**, 5930–5935 (2014).
64. Halpin, J. C. & Kardos, J. L. The Halpin-Tsai equations: a review. *Polym. Eng. Sci.* **16**, 344–352 (1976).
65. Holzapfel, G. A., Gasser, T. C. & Ogden, R. W. A new constitutive framework for arterial wall mechanics and a comparative study of material models. *J. Elast.* **61**, 1–48 (2000).
66. Lee, J. N., Park, C. & Whitesides, G. M. Solvent compatibility of poly (dimethylsiloxane)-based microfluidic devices. *Anal. Chem.* **75**, 6544–6554 (2003).
67. Thérien-Aubin, H., Wu, Z. L., Nie, Z. & Kumacheva, E. Multiple shape transformations of composite hydrogel sheets. *J. Am. Chem. Soc.* **135**, 4834–4839 (2013).
68. Morales, D. et al. Ionoprinted multi-responsive hydrogel actuators. *Micromachines* **7**, 98 (2016).
69. Wehner, M. et al. Pneumatic energy sources for autonomous and wearable soft robotics. *Soft Robot.* **1**, 263–274 (2014).

Acknowledgements

The authors gratefully acknowledge support from the Army Research Office, grant number W911NF-17-1-0147 and from the School of Engineering and Applied Science at the University of Pennsylvania. The authors thank Prof. Karen I. Winey and Lu Yan for use of and assistance with the tensile testing machine, Prof. Jason A. Burdick and Jonathan H. Galarraga for use of and assistance with the rheometer, Dr. A. Sydney Gladman for helpful discussions about printing hydrogels, Chengyang Mo for assistance with the high-speed camera, and Avinash Sooriyarachchi and Cindy Huang for their efforts on an earlier attempt of this work.

Author contributions

J.R.R. conceived the project; Y.J. and L.M.K. performed experiments; Y.J. performed numerical simulations. All authors contributed in writing the paper.

Additional information

Supplementary Information accompanies this paper at <https://doi.org/10.1038/s41467-018-08055-3>.

Competing interests: The authors declare no competing interests.

Reprints and permission information is available online at <http://npj.nature.com/reprintsandpermissions/>

Journal peer review information: *Nature Communications* thanks the anonymous reviewers for their contributions to the peer review of this work. Peer Reviewer Reports are available.

Publisher's note: Springer Nature remains neutral with regard to jurisdictional claims in published maps and institutional affiliations.



Open Access This article is licensed under a Creative Commons Attribution 4.0 International License, which permits use, sharing, adaptation, distribution and reproduction in any medium or format, as long as you give appropriate credit to the original author(s) and the source, provide a link to the Creative Commons license, and indicate if changes were made. The images or other third party material in this article are included in the article's Creative Commons license, unless indicated otherwise in a credit line to the material. If material is not included in the article's Creative Commons license and your intended use is not permitted by statutory regulation or exceeds the permitted use, you will need to obtain permission directly from the copyright holder. To view a copy of this license, visit <http://creativecommons.org/licenses/by/4.0/>.

© The Author(s) 2019

Supplementary Information

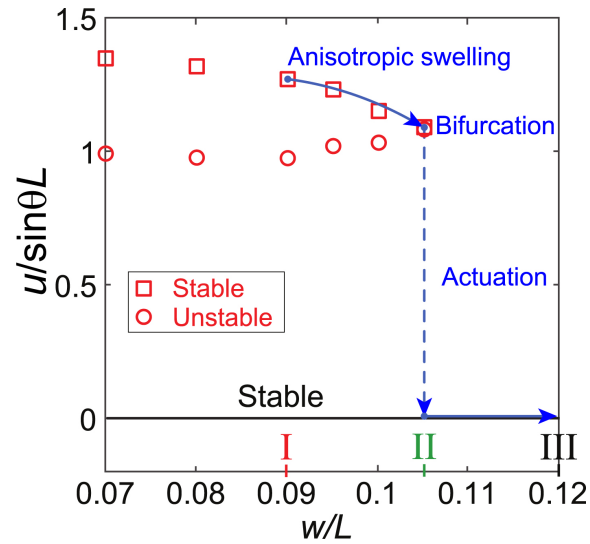
Bifurcation-based embodied logic and autonomous actuation

Yijie Jiang, Lucia M. Korpas, and Jordan R. Raney*

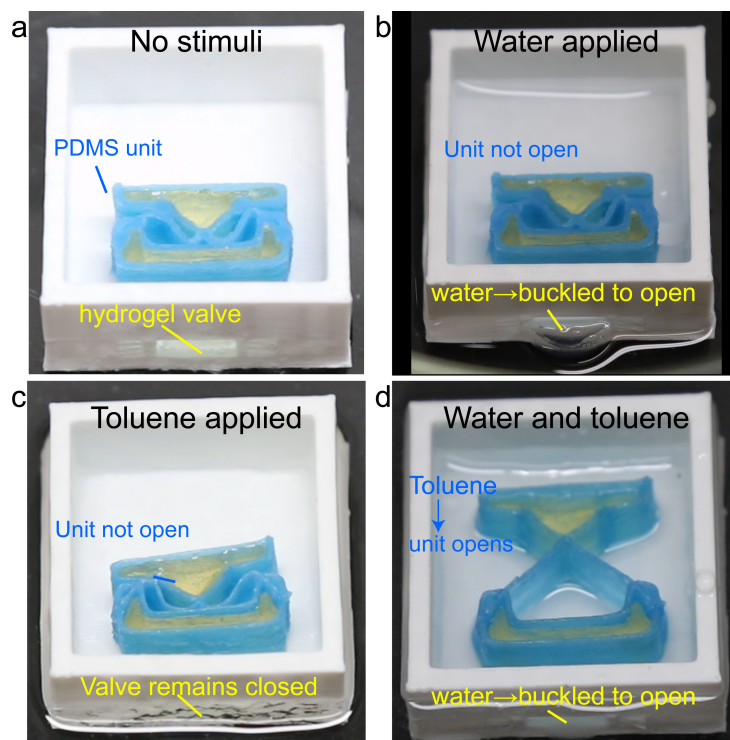
Department of Mechanical Engineering and Applied Mechanics, 220 S 33rd St., University of Pennsylvania, Philadelphia, PA 19104, USA

Corresponding author: Jordan R. Raney raney@seas.upenn.edu

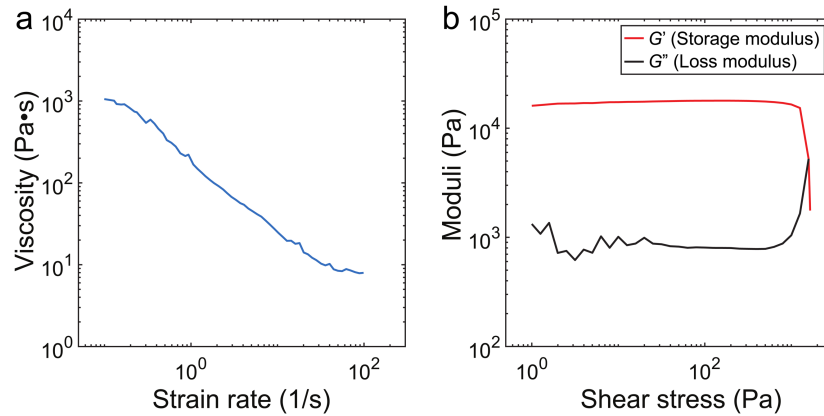
Supplementary Figures



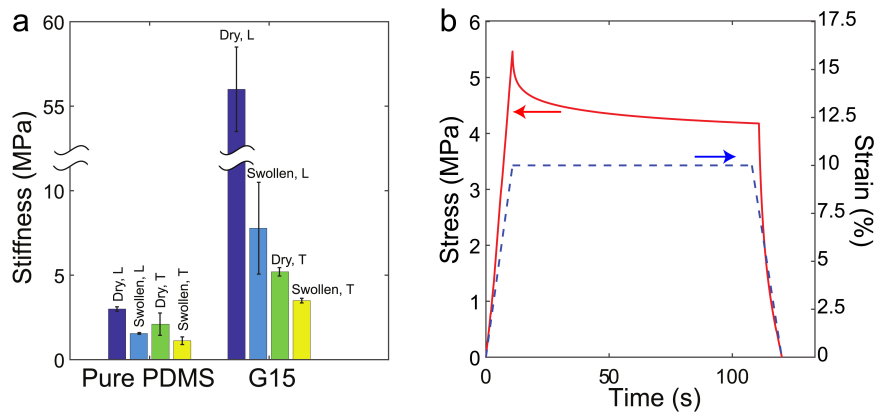
Supplementary Figure 1 | Bifurcation diagram for the geometric parameter w/L . The diagram is derived from finite element simulations and indicates the normalized displacements at which critical points (local energy minima and maximum) exist. The arrow illustrates how anisotropic swelling could lead to actuation due to bifurcation. The positions of Roman numerals (I-III) correspond to those in Fig. 1c.



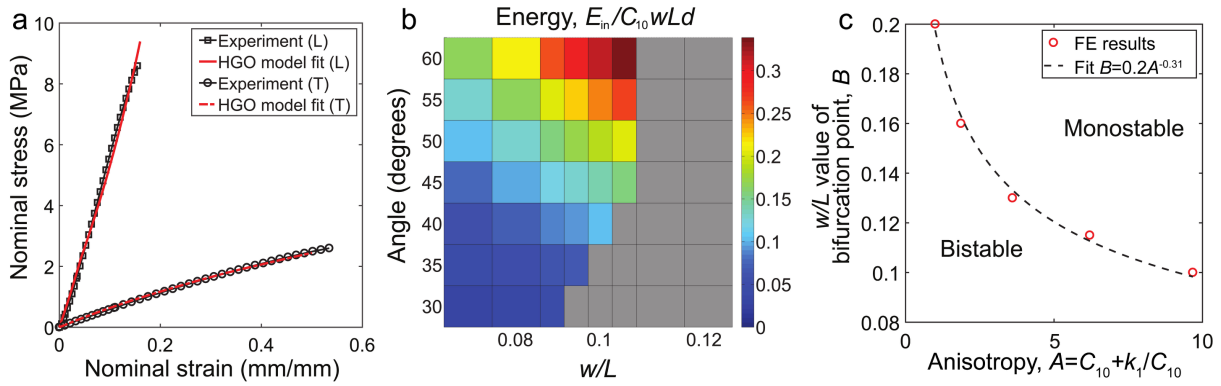
Supplementary Figure 2 | Demonstration of AND gate behavior. The box has a PDMS unit inside and a hydrogel valve, which is closed. When exposed to water, the hydrogel swells and buckles to open the valve, allowing solvent to go into the box. **(a)** No stimuli are present. **(b)** When there is only water, the valve opens and the water reaches the inner unit, but it cannot actuate the unit. **(c)** When only toluene is applied, the hydrogel valve remains closed and the toluene cannot reach the inner unit. **(d)** When water and toluene are both applied, the valve opens, toluene and water go into the box, and the toluene is absorbed into the unit, causing actuation to occur.



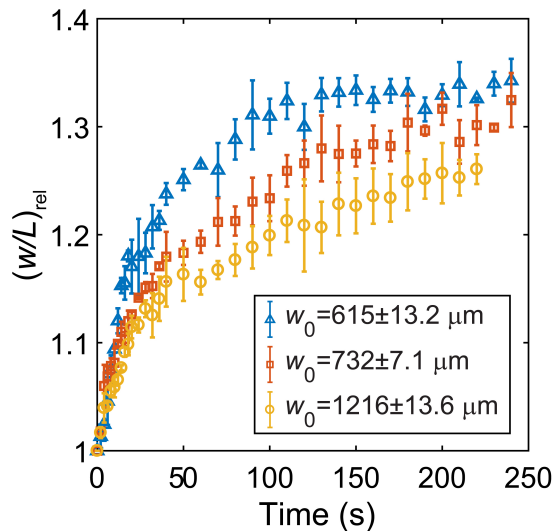
Supplementary Figure 3 | The rheological properties of hydrogel-cellulose fibril ink. It possesses a rheology that **(a)** is shear-thinning (exhibits a decrease in the apparent viscosity with increasing strain rate) and **(b)** includes a viscoelastic yield stress behavior, with a pronounced drop in the storage modulus at high shear stress.



Supplementary Figure 4 | Additional mechanical measurements on PDMS-GF15 material. **(a)** Results of tensile tests on dry and solvent-swollen tensile bars printed in longitudinal and transverse directions for both pure PDMS and PDMS-GF15 inks. **(b)** Stress relaxation tests for the PDMS-GF15 composite.

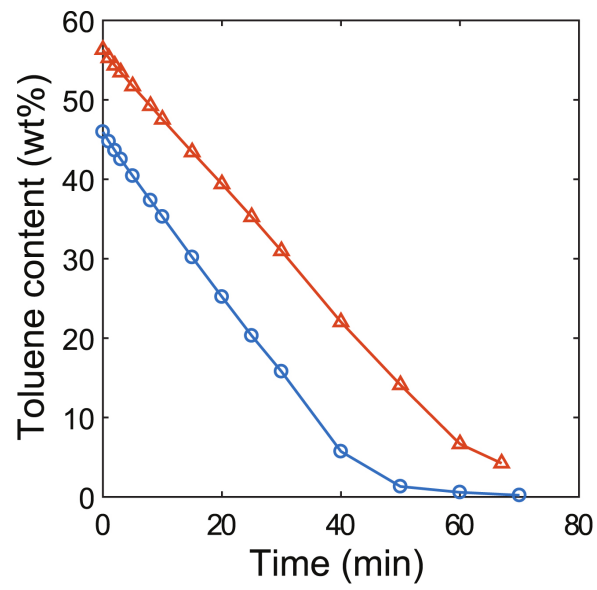


Supplementary Figure 5 | Finite element mechanical model and bistability simulations. (a) Nominal tensile stress-strain curves for PDMS-GF15 materials printed longitudinally (fibers parallel with loading) and transversely (fibers perpendicular to loading) and fitted using the HGO model. **(b)** Strain energy of the elastic beam at the peak of the energy barrier between the two stable states. The gray area indicates a monostable beam (only stable at $u=0$). **(c)** The location of the bifurcation point, B , as a function of material anisotropy as predicted by the HGO model (for a beam tilted at 45°), empirically following power law behavior.



Supplementary Figure 6 | The relative change in w/L for PDMS-GF15 beams as a function of time.

The measurements are for three beams with different initial widths. The error bars are the standard deviation of three measurements.



Supplementary Figure 7 | Evaporation of toluene from PDMS-GF15 beams. Measurement of the weight percentage of toluene in soaked samples evaporating in ambient as a function of time.

Supplementary Tables

Supplementary Table 1 Measurements of w for two PDMS-GF15 beams before submerging in toluene and after toluene is fully evaporated.

Beam #	Beam width (μm)	
	Before Toluene	After Toluene evaporation
1	775.4 ± 28.95	725.4 ± 43.63
2	759 ± 39.24	764.3 ± 28.06

Supplementary Table 2 Repeatability of actuation of PDMS-GF15 units. At least 70 min (ambient) was allowed between each test to ensure evaporation of all toluene.

Sample #	Repetitions	Actuation time (s)
1	11	34.42 ± 6.13
2	11	16.34 ± 3.74
3	11	2.27 ± 0.92
4	6	11.24 ± 3.97
5	6	3.05 ± 0.54

Supplementary Notes

Supplementary Note 1: DIW 3D printing

Direct ink writing (DIW) is an extrusion-based 3D printing technique^{1,2} in which material is extruded from a translating deposition nozzle at ambient conditions, relying on non-Newtonian material rheology to produce a pattern that maintains its shape after extrusion (Supplementary Figure 3). By decoupling the patterning step from the material cross-linking step, it offers a materials flexibility that allows us to meet all four criteria listed in the main text. For this approach to work it is important that the material is shear-thinning (to facilitate easy extrusion from a fine nozzle), and that it possesses a viscoelastic yield stress (so that the material maintains its shape after it is deposited). Subsequent immobilization steps (thermal or UV crosslinking, sintering, etc.) can then be taken after the pattern is formed, as appropriate for the specific material, to obtain the desired materials properties.

Supplementary Note 2: Additional mechanical measurements on PDMS-based composites

Tensile bars using pure PDMS and PDMS-GF15 inks were fabricated by direct ink writing. Both longitudinal and transverse samples were prepared (i.e., fibers oriented parallel with and perpendicular to the loading direction, respectively). After curing, some samples (referred to as “swollen” in Supplementary Figure 4a) were soaked in solvent (toluene) for 24 h, and other samples were not exposed to solvent (“dry” in Supplementary Figure 4a). Subsequently, an Instron Model 5564 was used to perform tensile tests on these samples in displacement control at a nominal strain rate 0.01 s^{-1} for all samples. Three samples were tested for each case (Supplementary Figure 4a). The swollen samples, infused with solvent, showed lower stiffness compared with the dry samples, but in both cases the materials remained highly anisotropic (i.e., for the G15 case in Supplementary Figure 4a notice the decrease in stiffness going from “Dry, L” to “Dry, T” but also going from “Swollen, L” to “Swollen, T”). We also conducted stress relaxation tests (Supplementary Figure 4b) to confirm that the material was sufficiently elastic to maintain the modest strains associated with buckling without prohibitive viscoelastic relaxation. An Instron MicroTester Model 5848 was used, with a ramp to 10% strain, followed by a hold for 100 s and

subsequent unloading. Stress relaxation was observed during the hold (Supplementary Figure 4b), such that the stress, σ , could be approximated by a power-law function, $\sigma = Kt^m$. For pure PDMS and PDMS-GF15 inks, the fitted exponents are $m_{\text{PDMS}} = -0.0095 \pm 0.0016$ and $m_{\text{GF15}} = -0.023 \pm 0.008$, respectively. Stress relaxation tests were performed at material strains comparable to those experienced during buckling, and these indicate a stable elastic response, ensuring that the beams can store elastic strain energy in a buckled configuration without prohibitive relaxation, as they must prior to actuation.

Supplementary Note 3: Halpin-Tsai model for short fiber composites

The Halpin-Tsai model^{3,4} is a micromechanics model commonly used for composites that include short, aligned fibers. It provides expressions for the stiffness along two principal directions relative to the fiber direction: longitudinal (L, parallel with fibers) and transverse (T, perpendicular to the fibers):

$$E_i = E_m \frac{1 + \beta_i \xi_i f}{1 - \beta_i f} \quad (1)$$

where f is the volume fraction of fibers, E_f and E_m are the Young's modulus of the fibers and the matrix, respectively, i indicates the direction (either L or T), and β_i is defined as

$$\beta_i = \frac{E_f/E_m - 1}{E_f/E_m + \xi_i} \quad (2)$$

L_f and d_f are the length and diameter of the fibers, respectively, and we use $\xi_L = 10$ in our fitting. For the PDMS-based composite with 15 vol% glass fibers (PDMS-GF15), when the values for E_f and E_m are obtained from fitting the longitudinal and transverse experimental data to Supplementary Equation (1) and (2), the results are $E_f = 52.13$ GPa and $E_m = 2.96$ MPa. Both values are consistent with glass and PDMS material properties.

Supplementary Note 4: Experimentally-determined phase boundary

To determine the phase boundary experimentally, we fabricated samples with a fixed angle of 45° and systematically-varying w/L ratios. Each sample was manually compressed to the buckled state and then released. Bistable samples remained in their buckled configuration, while monostable samples snapped

back to their undeformed configuration upon release of the load. We found that the maximum w/L for bistable units (with beam angle 45°) was 0.102 and the minimum w/L for monostable units was 0.108. Thus, we determined the phase boundary is $0.102 < w/L < 0.108$ (with fabrication inconsistencies causing the range).

Supplementary Note 5: Finite element analysis (FEA) on anisotropic bistable structures

Prior work⁵ determined the relationship between beam geometries (θ and w/L) and the stability behavior (bistable or monostable) for isotropic material. However, in addition to geometric parameters, the degree of material anisotropy also influences the stability. As a result, the geometric boundaries between behavioral regimes (e.g., bistable vs. monostable) that were determined previously are not universal and do not apply to anisotropic materials. Therefore, we used FEA to locate the boundary between regions of monostability and bistability in the geometric phase diagram (Fig. 1d) for the more general case in which the material anisotropy is allowed to vary. Before simulating the beams, we first fit an anisotropic hyperelastic mechanical model, the Holzapfel-Gasser-Ogden (HGO) model⁶, which expresses the strain energy as

$$U = C_{10}(\bar{I}_1 - 3) + \frac{1}{D} \left(\frac{(J^{\text{el}})^2}{2} - \ln J^{\text{el}} \right) + \frac{k_1}{2k_2} \sum_{\alpha=1}^N \{ \exp[k_2 \langle \bar{E}_\alpha \rangle^2] - 1 \} \quad (3)$$

with

$$\bar{E}_\alpha \stackrel{\text{def}}{=} \kappa(\bar{I}_1 - 3) + (1 - 3\kappa)(\bar{I}_{4(\alpha\alpha)} - 1) \quad (4)$$

where U is the strain energy per unit volume, C_{10} , D , k_1 , k_2 , and κ are material parameters that determine the mechanical behavior and need to be provided by the user. More details about this model and the detailed definitions of the other parameters can be found in the Abaqus manual.

To determine the parameters for the PDMS-GF15 material, tensile tests in both the longitudinal and transverse directions were simulated using a range of HGO material parameters, generating stress-strain curves that were fit to the experimental stress-strain data (Supplementary Figure 5a). The best-fit

parameters were $C_{10}=1.1525$ MPa, $D=7.805\times 10^{-3}$ MPa⁻¹, $k_1=10$ MPa, $k_2=0.01$, and $\kappa=0$ (see Supplementary Figure 5a). The anisotropy of the material can be indicated by $(C_{10}+k_1)/C_{10}$ with larger values of k_1 corresponding to increasing anisotropy. If $k_1=0$, the material is isotropic.

Beams with different w/L and tilt angle θ were modeled in Abaqus/Explicit[®] (version 6.9) using 2D plane strain models with CPE4R elements. The beams had fixed length 10 mm, systematically varied w/L from 0.07 to 0.12, and θ from 30° to 60°. Each tilted beam had one fixed end and was deformed by applying a vertical displacement to the other end, while constraining the horizontal displacement. The results of simulations of a tilted beam ($\theta=45^\circ$) with w/L varying from 0.07 to 0.12 are shown in Fig. 3a and 3b. The strain energy is normalized as $E/(C_{10}wLd)$, the force is normalized as $F/(C_{10}\cos\theta Ld)$, and the displacement is normalized as $u/(L\sin\theta)$, where C_{10} is a fitting parameter in the HGO model and d is the out-of-plane thickness of the beam, which is set to unity. A beam is bistable if its strain energy, simulated as a function of displacement, is found to have a second energy minimum for some nonzero value of u . For the value of C_{10} corresponding to the 15 vol% PDMS-GF material, and with a beam angle of $\theta=45^\circ$, the FEA shows that the beam is bistable if w/L is less than 0.105, and monostable otherwise. This FEA result is consistent with our observations with the 3D printed beam structures, for which we have experimentally determined a phase boundary between $0.102 < w/L < 0.108$ for $\theta=45^\circ$. We can develop a more complete phase diagram using FEA by systematically varying θ and w/L . We plot the FEA results of the strain energy of the elastic beam at the peak of the energy barrier, relative to the two stable morphologies (E_{in} indicates the strain energy of the peak relative to the unstrained beam at $u=0$ and E_{out} indicates the peak energy relative to the second, higher-energy stable state, as shown schematically in Fig. 1b). These quantities are normalized as $E_{in}/(C_{10}wLd)$ in Supplementary Figure 5b and $E_{out}/(C_{10}wLd)$ in Fig. 3c. The grey areas indicate regions of monostability while the different colors indicate bistability (i.e., E_{out} exists and is greater than 0). We performed a parametric study to determine the effect of the degree of anisotropy on the location of the bifurcation, B for different θ and w/L (forming phase boundaries). With increasing material anisotropy, the w/L value of the boundary at a given angle decreases as a power law function (see Supplementary

Figure 5c for the case $\theta=45^\circ$). For a beam of fixed length, L , the greater the degree of material anisotropy, the thinner the beam must be to be bistable. Figure 3d shows the bistable/monostable phase boundary for different degrees of material anisotropy: the isotropic case ($k_1=0$) is indicated by the black line, with increasing degrees of material anisotropy corresponding to larger values of k_1 . When we set $k_1=0$ (i.e., isotropic) in the HGO model, we recover the boundary expected for a Neo-Hookean isotropic material, as used in the previous study⁵. For the anisotropic material used here (e.g., the PDMS-GF15 ink), the boundary for a beam with a 45° tilt angle moves from $w/L = 0.2$ for an isotropic material to $w/L = 0.105$, i.e., nearly a factor of two.

Supplementary Note 6: Beam swelling measurements

Once the material is fully saturated by the solvent, the swelling is at a maximum such that, for an isotropic material, every linear dimension will have increased by the same factor. This factor is the *swelling ratio*, $\eta=x_s/x_0$ (where x_0 indicates the initial length of the material along some linear dimension and x_s indicates the length along that same dimension after the material is completely saturated with solvent). The value of the swelling ratio is unique to each material-solvent combination, based on the chemical affinity.

Three PDMS-GF15 beams with different initial widths were fabricated and submerged in toluene. The values of w and L were recorded as a function of time by recording video using an optical microscope (Amscope[®] MU1000) and post-processing using ImageJ. Time $t=0$ is defined as the first stable frame after the toluene was added. As shown in Supplementary Figure 6, $(w/L)_{rel}=(w/L)/(w_0/L_0)$ increases quickly initially and then converges to a constant value at longer times. Since the diffusion time depends on the amount of material through which the solvent must diffuse, the initial beam width affects when the equilibrium value is reached. To determine swelling at saturation, microscope images were taken before and after one day of submersion in toluene, allowing assessment of initial and final geometries using ImageJ.

Supplementary Note 7: Beam swelling model and estimated actuation time

When there is enough solvent for a material to absorb, the material eventually becomes fully saturated with the solvent, defining the saturation time, t_s (which depends on the beam volume through which the solvent diffuses). For $t \geq t_s$, the quantity $(w/L)_{\text{rel}}$ therefore does not change, remaining constant at a value corresponding approximately to the swelling ratio for the specific material-stimulus combination, η_T/η_L . For the time prior to this ($t < t_s$), we model the observed changes to $(w/L)_{\text{rel}}$ by assuming a mechanism of simple diffusion. The beams are printed with significant out-of-plane thickness, d (see photos of physical samples in Figs. 5 and 6). The solvent front is therefore assumed to diffuse inward from the two surfaces in the L - d plane, perpendicular to the long axis, L , and parallel with the direction of the beam width. Assuming simple diffusion, the location of the solvent front relative to these surfaces increases in depth, a , as

$$a = \sqrt{2Dt} \quad (5)$$

where D is the diffusion coefficient (e.g., of toluene in PDMS). The time at which the beam is entirely saturated, t_s , occurs when the two solvent fronts diffusing from the two surfaces meet in the middle of the beam, i.e., when $a=w_0/2$, which occurs at time

$$t_s = \frac{w_0^2}{8D} \quad (6)$$

We assume that as the front propagates into a new infinitesimal slice of the beam, dw , that portion of the beam immediately takes on the saturated dimensions $dw=\eta_T dw_0$. The length remains approximately L_0 since the swelling ratio in the longitudinal direction is very close to $\eta_L=1$ for our PDMS-GF15 material (Fig. 4a). Then the changing value of $(w/L)_{\text{rel}}=(w/L)/(w_0/L_0)$ follows the relationship

$$(w/L)_{\text{rel}} = \begin{cases} 1 + \sqrt{(t/t_s)}(\eta_T - 1), & t < t_s \\ \eta_T, & t \geq t_s \end{cases} \quad (7)$$

where η_T is the swelling ratios in the transverse direction (as found experimentally and shown in Fig. 4a).

By fitting our experimental measurements to this model as shown in Fig. 4c for PDMS-GF15 (see also the experimental data in Supplementary Figure 6), we find $D=(6.93\pm 0.5)\times 10^{-6} \text{ cm}^2\text{s}^{-1}$, which is close to the

value reported for toluene in a different type of PDMS^{7,8}. We use this to derive a time, \hat{t}^* , at which the model predicts that the beam geometry will reach the bifurcation point (i.e., the expected time of actuation). By noting that $w/L=B$ at $t=\hat{t}^*$ and expressing w/L as $(w_0/L_0)(w/L)_{rel}$, we combine Supplementary Equation (6) and (7) to find

$$\hat{t}^* = \frac{(BL_0 - w_0)^2}{8D(\eta_T - 1)^2} \quad (8)$$

Supplementary Note 8: Recovery and reusability of PDMS-based beams

Based on the robust cross-linking of PDMS, we expected that after exposure to solvent and subsequent drying that all solvent would leave the material and allow the beams to be reused. To confirm this, three sections of different PDMS-GF15 beams were first weighed, and dimensions were recorded. They were then soaked in toluene for ~1 day. Then the materials were removed from the toluene and placed on a digital scale to allow measurement of the mass as a function of time. Supplementary Figure 7 shows the gradual reduction of toluene content inside the beams (calculated based on the ratio of mass of toluene, taking the difference between the instantaneous measured mass and the original dry mass, to the instantaneous mass). It takes ~70 min for all toluene to evaporate. Supplementary Table 1 shows measurements of the width of two PDMS-GF15 beams before submerging into toluene and over about 70 min of evaporation time, showing complete recovery of the original geometry within the margin of error. After the toluene evaporates, the beams move from the swollen, monostable configuration back to their original bistable geometries. With these structures once again exhibiting bistability, they can be reused for autonomous actuation in experiments.

Supplementary Note 9: Ink preparation

PDMS-based inks

PDMS (SE 1700 and Sylgard[®] 184, Dow Corning Co.) and glass fibers (Fibre Glast Co.) are mixed (SpeedMixer[™], FlackTek, Inc) at 1500 rpm for 45 s, 1800 rpm for 30 s and 1200 rpm for 2 min under 20 Torr vacuum. The ratio of SE 1700 to Sylgard[®] 184 is 85:15 for 0 and 5 vol% glass fiber ink, and 83:17

for 10, 12, and 15 vol% glass fiber inks. The base to cross linker ratio is 10:1 for both SE 1700 and Sylgard[®] 184. The glass fibers are observed to be ~540 μm in length and 14.6 ± 1.53 μm in width as received from the manufacturer, but the length decreases to 72.9 ± 17.3 μm during mixing. The mixed ink is then transferred to a syringe and centrifuged (ST 8 Centrifuge, Thermo Scientific[®]) at 3400 rpm for 13 min, and a deposition nozzle is connected to the syringe barrel via Luer lock (Nordson EFD[®]). In this study, nozzles with an inner diameter of 410 μm are used for all PDMS-based ink printing.

Hydrogel-based inks

First, nanofibrillated cellulose (NFC) is diluted in DI water, which is deoxygenated under nitrogen flow for 30 min, and mixed at 800 rpm for 15 s and 1500 rpm for 1 min in a capped container. Synthetic hectorite clay (Laponite XLG) is then added under nitrogen flow and mixed at 1800 rpm for 3 min and 1500 rpm for 2 min. The clay solution is additionally hand mixed if white aggregates are seen. N-isopropylacrylamide (NIPAm) is then added to the clay solution under nitrogen flow and mixed again at 1800 rpm for 3 min and 1500 rpm for 2 min. Irgacure 2959, the ultraviolet photoinitiator, is added and the ink is mixed at 1500 rpm for 2 min. The mass percentage of these components are DI water: NFC: Laponite clay: NIPAm: Irgacure= 81: 0.77: 10: 8.1: 0.12. Finally, 5 wt% PDMS (Sylgard[®] 184 with 10% crosslinker) is added and mixed at 800 rpm for 1 min. The mixed ink is then transferred to a syringe and centrifuged at 3400 rpm for 13 min. A metal straight nozzle with outlet diameter of 250 μm is used for hydrogel-based ink printing. Because the hydrogel has a more time-dependent mechanical response than the printed PDMS, it was more challenging to obtain the desired bistable response. To improve this, each hydrogel beam was actually fabricated as a composite: first, two parallel filaments of the hydrogel-based ink were printed, separated by a small amount (on the order of the filament width), then PDMS (Sylgard[®] 184) was extruded in between. The PDMS provided a more robust elastic response of the overall beam, but the hydrogel still fully enclosed the PDMS so that the composite beam only becomes swollen in the presence of water.

Supplementary Note 10: DIW printing

A ShopBot[®] D2418 3D translation stage is used for control of movement of the syringe in 3D. Print paths are controlled by G-code or ShopBot[®] (G-code derivative) commands, which are generated by Python or Matlab[®] scripts. A volumetric dispenser (Ultra[™] 2800, Nordson) or a pressure control box (EFD[®] Ultim[™] V) is used for control of ink extrusion flow rate. Samples are printed on a substrate of Teflon-coated aluminum foils at ambient temperature. PDMS-based samples are cured in an oven (HERA[™]Therm, Thermo Scientific[®]) at 100 °C for 1 h. Hydrogel-based samples are cured via UV crosslinking (~60 mW/cm² for 300 s in OmniCure[®] Series 2000). Systems that include both materials are first UV cured and then thermally cured at 60 °C for 4 h in a capped container. In order to provide the desired boundary conditions for the beams, epoxy (Epon 828, resin:cross linker=3:1) was cast and cured at room temperature for more than 6 hours to provide rigid boundaries for both ends of each PDMS beam. The hydrogel-based units were mounted on 3D printed polylactic acid (PLA) pieces, to provide appropriate boundary conditions. After completing these steps, we found that approximately 80% of the specimens possessed the desired mechanical functionality, while the other 20% did not. This yield rate is significantly lower than our previous work using isotropic materials. This therefore seems to be a result of the use of fibers (e.g., the fibers can partially clog the nozzle, producing clumping of the fibers in the material; the presence of fibers also roughens the surface of the beams; these inhomogeneities affect the mechanical properties; the higher the volume fraction, the more of an issue this becomes).

Supplementary References

1. Raney, J. R. & Lewis, J. A. Printing mesoscale architectures. *MRS Bull.* **40**, 943–950 (2015).
2. Lewis, J. A. Direct ink writing of 3D functional materials. *Adv. Funct. Mater.* **16**, 2193–2204 (2006).
3. Halpin, J. C. Effects of Environmental Factors on Composite Materials. *Tech. Rep. Afml-Tr-67-423* (1969).
4. Halpin, J. C. & Kardos, J. L. The Halpin-Tsai equations: A review. *Polym. Eng. Sci.* **16**, 344–352 (1976).
5. Shan, S. *et al.* Multistable Architected Materials for Trapping Elastic Strain Energy. *Adv. Mater.* **27**, 4296–4301 (2015).
6. Holzapfel, G. A., Gasser, T. C. & Ogden, R. W. A new constitutive framework for arterial wall mechanics and a comparative study of material models. *J. Elast.* **61**, 1–48 (2000).
7. Chao, K. P., Wang, V. S., Yang, H. W. & Wang, C. I. Estimation of effective diffusion coefficients for benzene and toluene in PDMS for direct solid phase microextraction. *Polym. Test.* **30**, 501–508 (2011).
8. Alexander, M., Boscaini, E., Lindinger, W. & Märk, T. D. Membrane introduction proton-transfer reaction mass spectrometry. *Int. J. Mass Spectrom.* **223–224**, 763–770 (2003).